Photochemistry of oxidized Hg(I) and Hg(II) species suggests missing mercury oxidation in the troposphere

Alfonso Saiz-Lopez[a,1], Oleg Travnikov[b,1], Jeroen E. Sonke[c], Colin P. Thackray[d], Daniel J. Jacob[d], Javier Carmona-García[e], Antonio Francés-Monerris[f,g], Daniel Roca-Sanjuán[e], A. Ulises Acuña[a], Juan Z. Dávalos[a], Carlos A. Cuevas[a], Martin Jiskra[c,h], Feiyue Wang[i], Johannes Bieser[j], John M. C. Plane[k], and Joseph S. Francisco[l,m,1]

[a]Department of Atmospheric Chemistry and Climate, Institute of Physical Chemistry Rocasolano, Spanish National Research Council (CSIC), 28006 Madrid, Spain; [b]Meteorological Synthesizing Centre–East of EMEP, 115419 Moscow, Russia; [c]Géosciences Environnement Toulouse, CNRS/Observatoire Midi-Pyrénées (OMP)/Université de Toulouse, 31400 Toulouse, France; [d]Harvard John A. Paulson School of Engineering and Applied Sciences, Harvard University, Cambridge, MA 02138; [e]Institut de Ciència Molecular, Universitat de València, 46071 València, Spain; [f]Departamento de Química Física, Universitat de València, 46100 València, Spain; [g]Université de Lorraine, CNRS, Laboratoire de Physique et Chimie Théoriques (LPCT), F-54000 Nancy, France; [h]Department of Environmental Sciences, University of Basel, 4056 Basel, Switzerland; [i]Department of Environment and Geography, Centre for Earth Observation Science, University of Manitoba, Winnipeg, MB R3T 2N2, Canada; [j]Helmholtz-Zentrum Geethacht, Institute of Coastal Research, 21502 Geesthacht, Germany; [k]School of Chemistry, University of Leeds, LS2 9TJ Leeds, United Kingdom; [l]Department of Earth and Environmental Science,University of Pennsylvania, Philadelphia, PA 19104; and [m]Department of Chemistry, University of Pennsylvania, Philadelphia, PA 19104

Contributed by Joseph S. Francisco, October 26, 2020 (sent for review December 27, 2019; reviewed by Michael E. Goodsite and Anthony J. Hynes)

Mercury (Hg), a global contaminant, is emitted mainly in its elemental form Hg^0 to the atmosphere where it is oxidized to reactive Hg^{II} compounds, which efficiently deposit to surface ecosystems. Therefore, the chemical cycling between the elemental and oxidized Hg forms in the atmosphere determines the scale and geographical pattern of global Hg deposition. Recent advances in the photochemistry of gas-phase oxidized Hg^I and Hg^{II} species postulate their photodissociation back to Hg^0 as a crucial step in the atmospheric Hg redox cycle. However, the significance of these photodissociation mechanisms on atmospheric Hg chemistry, lifetime, and surface deposition remains uncertain. Here we implement a comprehensive and quantitative mechanism of the photochemical and thermal atmospheric reactions between Hg^0, Hg^I, and Hg^{II} species in a global model and evaluate the results against atmospheric Hg observations. We find that the photochemistry of Hg^I and Hg^{II} leads to insufficient Hg oxidation globally. The combined efficient photoreduction of Hg^I and Hg^{II} to Hg^0 competes with thermal oxidation of Hg^0, resulting in a large model overestimation of 99% of measured Hg^0 and underestimation of 51% of oxidized Hg and ∼66% of Hg^{II} wet deposition. This in turn leads to a significant increase in the calculated global atmospheric Hg lifetime of 20 mo, which is unrealistically longer than the 3–6-mo range based on observed atmospheric Hg variability. These results show that the Hg^I and Hg^{II} photoreduction processes largely offset the efficiency of bromine-initiated Hg^0 oxidation and reveal missing Hg oxidation processes in the troposphere.

atmospheric chemistry | gas-phase mercury reactivity | tropospheric chemistry | mercury photoreduction | atmospheric modeling

Annually, about 8 Gg of mercury (Hg) are released to the atmosphere from present-day anthropogenic (∼39%) and natural (∼6%) sources, and reemissions of previously deposited Hg from natural and anthropogenic sources (∼55%) (1). The average concentration of Hg in the atmosphere is relatively low, in the range of 1–2 ng/m^3 (equivalent to ∼100–200 parts per quadrillion mixing ratio). Earth's atmosphere is therefore a minor Hg reservoir of ∼5 Gg, compared with terrestrial soil and marine Hg pools (1,450 and 280 Gg, respectively) (2). However, the atmosphere is a key component of the global Hg cycle because it facilitates the planetwide dispersion of the metal. This global dynamic is governed by a complex combination of emissions, atmospheric chemical processing, transport, and surface deposition (3, 4). In the atmosphere, Hg cycles between elemental Hg^0 and oxidized monovalent Hg^I and divalent Hg^{II} forms (5, 6). Oxidation mechanisms of atmospheric Hg have been reviewed several times [e.g., Si and Ariya, 2018 (7) and references therein]. The current view is that the slow gas-phase oxidation of Hg^0 by hydroxyl radical (OH) (8) and ozone (O_3) is frequently complemented or replaced by the much more efficient oxidation by atomic bromine (Br) (9, 10). Although the knowledge of the amount and distribution of tropospheric Br has improved during the last decade (11, 12), more measurements of tropospheric Br concentrations and their spatial distribution are sorely needed to reduce uncertainty in atmospheric kinetic and transport models of Hg oxidation based on Br chemistry.

Mercury is released to the atmosphere mostly as gaseous elemental Hg^0, which is currently assumed to be oxidized to Hg^{II} by a two-step mechanism (6, 9, 10, 13). The first step is initiated by photochemically produced Br atoms to form HgBr, a radical Hg^I intermediate that can then photolytically or thermally decompose back to Hg^0, or be further oxidized to Hg^{II} compounds by atmospheric radicals such as NO_2, HO_2, Br, OH, I, Cl, BrO, ClO, and IO (6, 9, 13, 14). Based on this scheme, and despite Br

Significance

The atmospheric chemistry of mercury, a global priority pollutant, is key to its transport and deposition to the surface environment. Assessments of its risks to humans and ecosystems rely on an accurate understanding of global mercury cycling. This work shows that the chemical reactions and rates currently employed to interpret Hg chemistry in the atmosphere fails to explain observed atmospheric mercury concentrations and deposition. We report that model simulations incorporating recent developments in the photoreduction mechanisms of the oxidized forms of mercury (Hg^I and Hg^{II}) lead to a significant model underestimation of global observations of these oxidized species in the troposphere and their surface wet deposition. This implies that there must be currently unidentified mercury oxidation processes in the troposphere.

Author contributions: A.S.-L. and J.S.F. designed research; A.S.-L., O.T., J.E.S., and A.U.A. performed research; A.S.-L., O.T., J.E.S., C.P.T., D.J.J., J.C.-G., A.F.-M., D.R.-S., A.U.A., J.Z.D., C.A.C., M.J., F.W., J.B., J.M.C.P., and J.S.F. analyzed data; and A.S.-L. and J.S.F. wrote the paper.

Reviewers: M.E.G., University of Adelaide; and A.J.H., University of Miami.

The authors declare no competing interest.

[1]To whom correspondence may be addressed. Email: a.saiz@csic.es, Oleg.Travnikov@msceast.org, or frjoseph@sas.upenn.edu.

This article contains supporting information online at https://www.pnas.org/lookup/suppl/doi:10.1073/pnas.1922486117/-/DCSupplemental.

First published November 23, 2020.

being a minor atmospheric constituent, Holmes et al. (14) proposed that Hg^0 oxidation by Br is potentially the dominant oxidation pathway at a global scale. Field and model studies have reported evidence of the Br-initiated oxidation over different environments where Br chemistry is active and relatively abundant such as the polar regions [e.g., ref. (15)], salt lakes [e.g., ref. (16)], tropical marine boundary layer (13) and free troposphere (17). Several models, however, still consider Hg^0 oxidation by O_3 and OH as the main pathway (18, 19), particularly in the continental atmosphere.

Once oxidized, gaseous Hg^{II} species are more water soluble and particle reactive, and eventually partition into aerosols and clouds, before efficient deposition to the Earth's surface by wet and dry deposition processes. Recent theoretical work has shown that divalent (Hg^{II}: *syn*-HgBrONO, *anti*-HgBrONO, HgBrOOH, HgBrOH, $HgBrNO_2$, $HgBr_2$, $HgCl_2$, HgBrOCl, HgBrI, HgBrOBr, HgBrOI) (20) and monovalent (Hg^{I}: HgBr, HgCl, HgOH, HgI) (21) species strongly absorb ultraviolet-visible light. Therefore, daytime solar radiation leads to efficient gas-phase photolysis, which can dominate Hg^{I} and Hg^{II} reduction in the atmosphere and shorten the lifetime of oxidized Hg species compared to previous reaction schemes where Hg reduction was restricted to the aqueous cloud phase (6). Experimental evidence of photoreduction of oxidized Hg has been reported from observations on the remote Tibetan Plateau (22) and in urban air (23). The rapid photodissociation of *syn*-HgBrONO has been suggested to produce the HgBrO radical, which upon reaction with volatile organic compounds swiftly forms HgBrOH (24). Finally, a recent computational study has reported quantitative photodissociation channels and photoproducts of the likely major gaseous oxidized Hg^{II} compounds (*syn*-HgBrONO, HgBrOOH, HgBrO, and HgBrOH), and constructed a quantitative mechanism of the photochemical and thermal conversion between Hg^0, Hg^{I}, and Hg^{II} species in the atmosphere (25).

These recent theoretical works suggest that gas-phase photodissociation of oxidized $Hg^{I,II}$ is a key process in the global atmospheric cycling of this metal. However, the influence of these combined new photochemical mechanisms on the redox chemistry, lifetime, and surface deposition of Hg in the global atmosphere is currently unknown. Here, a state-of-the-art global Hg chemical transport model is used to evaluate the impact of the recently proposed Hg photoreduction mechanisms against atmospheric Hg measurements. The evaluation includes the different photodissociation processes for Hg^{I} and Hg^{II}, and their impact on atmospheric Hg concentrations and surface deposition patterns, lifetime, and vertical profiles in the troposphere.

Chemical Mechanisms and Global Model Simulations

Fig. 1 shows the main reactions for thermal and photochemical conversion between Hg^0, Hg^{I}, and Hg^{II} species (25). *syn*-HgBrONO and HgBrOOH are considered the major gaseous oxidized Hg^{II} species from Br-initiated two-step Hg^0 oxidation (6, 26, 27). It has been calculated that following gas-phase photolysis, *syn*-HgBrONO breaks down to HgBrO (90%) and HgBr (10%) (24, 25), and HgBrOOH yields Hg^0 (66%), HgBrO (31%), and HgBr (3%) (25). The computed tropospheric photolysis rate of the HgBrO radical ($2.95 \times 10^{-2}\cdot s^{-1}$) (25) is too slow to compete with the proposed reaction of the radical with methane [pseudo–first-order rate, $k' = 11\ s^{-1}$ at 298 K and 1 atm (24)] to form HgBrOH. Note that the equivalent reaction of HgBrO with NO_2 has a $k' = 2 \times 10^{-2}\cdot s^{-1}$ at 298 K and 1 atm (24). Therefore, the photolysis of *syn*-HgBrONO does not lead directly to photoreduction but to the formation, with a 90% yield, of another Hg^{II} species, namely HgBrOH. Photodissociation of HgBrOH results in Hg^0 (49%), HgOH (35%), and HgBr (15%). The resulting Hg^{I} photoproducts (HgBr and HgOH) will also efficiently photodissociate to Hg^0 (21). Summed together, the photolysis of *syn*-HgBrONO, HgBrOOH, and HgBrOH reduces oxidized $Hg^{I,II}$ to Hg^0 directly (38%) and indirectly (62%) (25). Hence, the overall combination of the different photodissociation pathways indicates that the suggested main gaseous oxidized Hg compounds, both Hg^{I} and Hg^{II}, rapidly return directly and indirectly to Hg^0 via gas-phase photolysis. This results in Hg^0 being the predominant product of oxidized $Hg^{I,II}$ gas-phase photoreduction in the atmosphere.

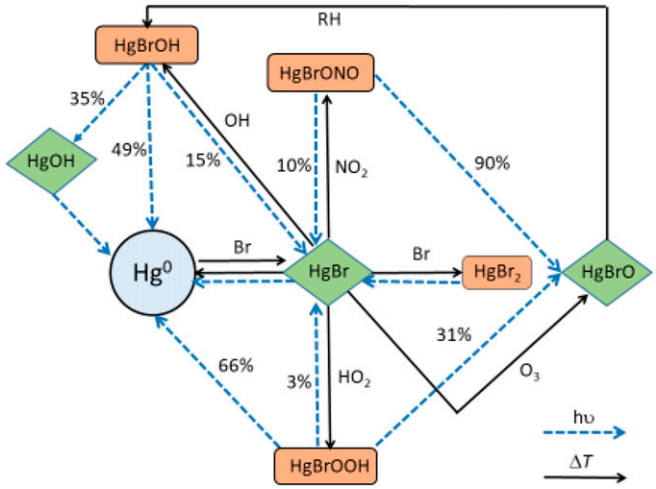

Fig. 1. Thermal and photochemical reactions of major mercury species in the atmosphere, including the Hg^{I} (green) and Hg^{II} (orange) photoreduction processes. The photoproduct yields are shown as percentage. The reaction HgBr + O_3 to yield HgBrO proposed in this work is discussed in detail in *SI Appendix, Supplementary Note 2*.

Recently, a large collaborative multimodel effort was conducted to investigate the impact of different Hg oxidation mechanisms (i.e., slow reaction with ozone and OH radical, and faster Br-initiated oxidation) and emissions on global Hg distributions (28, 29). However, the redox mechanisms tested in this multimodel evaluation did not consider the photoreduction of Hg^{I} and Hg^{II} species. To evaluate the global impact of these photoreduction mechanisms, and their competition with thermal Hg oxidation, we use the global chemical transport model GLEMOS (Global European Monitoring and Evaluation Program Multimedia Modeling System) (*Methods*). Several simulation tests (Table 1) were performed with the model using different combinations of the state-of-the-art chemical mechanisms. The first test (run 1) included the Br-initiated two-step oxidation of Hg^0, including oxidation by OH, with thermal reduction of Hg^{I} and no photoreduction of Hg^{I} and Hg^{II} (*Methods*, *SI Appendix*, Table S1, reactions **R1–R7**). The second test (run 2) consisted of the Br and OH oxidation chemistry and photodissociation of Hg^{I} and Hg^{II} according to the chemical scheme shown in Fig. 1 (see *SI Appendix*, Table S1, reactions **R1–R10**). We also conducted two model sensitivity runs to assess the influence of the uncertainties in the key thermal reaction and photolysis rates as reported in the literature. In the first run (run 2a, Table 1), we take the upper limit of the uncertainty in key oxidation reactions and the lower limit of the uncertainty in Hg reduction reactions. This is done to test maximum Hg oxidation within the limit of kinetic uncertainties. The opposite, i.e., minimum Hg oxidation within uncertainty, was tested in run 2b. The evaluation was focused on a comparison of modeled and measured concentrations of Hg^0, oxidized Hg (Hg^{I} + Hg^{II}), as well as Hg^{II} wet deposition. Model tests were carried out for the period 2007–2013 with the first 6 y as a model spin up and the year 2013 as the control run.

Table 1. Model runs

Run ID	Scenario
Run 1	Two-step Hg° oxidation by Br (**R1–R4**) and OH (**R5–R7**) [see chemical scheme in *SI Appendix*, Table S1], with no photolysis of Hg(I) and Hg(II) species.
Run 2	Two-step Hg° oxidation by Br (**R1–R4**) and OH (**R5–R7**), with photolysis of Hg(I) and Hg(II) species (**R8–R10**).
Run 2a	Run 2 with the value of reaction rates **R1–R10** that would maximize Hg° oxidation, within the published uncertainty.
Run 2b	Run 2 with the value of reaction rates **R1–R10** that would minimize Hg° oxidation, within the published uncertainty.
Run 3	Run 2 with new reaction **R11** (oxidation of HgBr by O_3 to form HgBrO).
Run 4	Run 2 with atmospheric bromine concentration increased by a factor of 2.

As mentioned above, the gas-phase oxidation of Hg^0 by O_3 ($Hg + O_3 \rightarrow HgO + O_2$) has been considered as a major oxidation pathway in the atmosphere. The rate coefficient for this reaction was measured to be $8.4 \times 10^{-17} \exp(-11.7 \text{ kJ mol}^{-1}/RT)$ cm^3 $\text{molecule}^{-1}\cdot\text{s}^{-1}$ (30), which implies a bond dissociation energy $D_0(HgO) \geq 88$ kJ mol^{-1}. However, high-level theoretical calculation shows that the Hg–O bond is in fact rather weak, with a reported value ~17 kJ mol^{-1} (31). This means that not only this reaction is too slow to effectively oxidize Hg in the troposphere, but also that any formed HgO has a high probability of promptly dissociating [for further details see the comprehensive discussion of Hynes et al. (32) and *SI Appendix*, *Supplementary Note 1*]. Therefore, here we do not consider gas-phase oxidation of Hg^0 by O_3. Similarly, due to the very rapid HgOH dissociation, the OH-initiated Hg^0 oxidation is considered not to be important (8, 9), although it is included in our simulations (*SI Appendix*, Table S1).

Impact of Hg^I and Hg^{II} Photoreduction on Simulated Hg Concentrations

The total atmospheric Hg burden and, as a consequence, air concentration of Hg species and their lifetime depend on both the Hg redox chemistry and on global emissions. The Hg lifetime against deposition in the model varies from 3.5 mo in run 1 without photoreduction to 20 mo in run 2 when photolysis of Hg^I and Hg^{II} species is included, with calculated lifetimes of 16.3 and 22.4 mo for sensitivity run 2a and run 2b, respectively (Table 2). From observed atmospheric variability of Hg, the lifetime against deposition should be in the range of 3–6 mo (6). The total Hg^0 mass increases by a factor of 5.7 from 1,390 Mg (run 1) to 7,865 Mg (run 2) (Table 2). This is due to photoreduction of (Hg^I + Hg^{II}) species back to Hg^0. The unrealistically long atmospheric lifetimes against deposition obtained in model runs 2, 2a, and 2b are confirmed by comparison of observed and simulated standard deviations (SDs) of Hg^0 concentrations across ground-based sites. We consider here the relative SD instead of the absolute one (6) due to considerable difference in mean concentration levels simulated in different tests. Model runs significantly deviate from Hg^0 ground-based measurements with 43% underestimation for run 1 and 99% overestimation for run 2 (Fig. 2 and Table 2). The short lifetime in run 1 leads to very low surface Hg^0 concentrations (0.3–1 ng m^{-3}). In contrast, application of the photoreduction mechanism in run 2 leads to much higher Hg^0 concentrations (2–3 ng m^{-3}), which overestimate observations by a factor of 2 (*SI Appendix*, Fig. S1).

Simulation of the chemical mechanism without $Hg^{I,II}$ photolysis (run 1) leads to a large overestimation (181%) of ground-based measurements of oxidized Hg (Fig. 3) despite underestimation of total Hg mass in the atmosphere (Table 2). In contrast, photoreduction of Hg^I and Hg^{II} (run 2) results in strong underestimation (51%) of oxidized Hg observations (Table 2). The model simulations considering the kinetics uncertainties, run 2a and run 2b, lead to underestimations of observed $Hg^{I,II}$ of 38 and 59%, respectively. Note that ground-based observations of oxidized Hg based on KCl-coated denuder techniques are associated with large uncertainty, and possibly biased low by up to one order of magnitude (33, 34). This low bias in Hg^{II} observations would indicate even stronger underestimation in run 2. Furthermore, a recent experimental study has reported the reaction rate constant of $HgBr + NO_2$ to HgBrONO to be 3–11 times lower than that predicted by theory (35), and incorporated in our model. Also, a new theoretical study, not included in this work, proposes the reduction of HgBrO by reaction with CO ($HgBrO + CO \rightarrow HgBr + CO_2$) (36). All of this implies that the model underestimation of Hg^{II} observations would be even larger with the inclusion of the results from these two very recent studies.

The effect of including photochemistry of oxidized $Hg^{I,II}$ is smaller near source regions, which are affected directly by anthropogenic emissions, and increase with distance from sources, in particular at low latitudes (Fig. 3 and *SI Appendix*, Fig. S2). We therefore note a marked regionality in the relative differences from the different model runs. Large increases of total Hg atmospheric mass from run 1 to run 2 partly compensate for the lack of oxidation capacity of the atmosphere. Nevertheless, the mass of global atmospheric $Hg^{I,II}$ decreases from 127 Mg (run 1) to 46 Mg (run 2) following efficient photoreduction (Table 2).

Mercury wet deposition is largely affected by the rate of Hg oxidation to yield soluble and particle-reactive $Hg^{I,II}$ species in the free troposphere. Comparison with measurements shows that implementation of the new photoreduction mechanism leads to a large underestimation (66%) of Hg wet deposition fluxes in North America and Europe (Fig. 4). The largest decrease occurs in the tropics and the smallest over source regions, mirroring the changes of oxidized Hg concentrations. The apparently correct estimation of wet deposition in run 1 (Table 2 and Fig. 4) is a consequence of the large overestimation (181%) of ground-level oxidized Hg.

More insight into the effect of photoreduction can be obtained from the analysis of vertical profiles of Hg^0 and oxidized Hg species (Fig. 5 and *Methods*). The difference in chemical mechanisms leads to significant differences between the modeled Hg^0 vertical profiles and the measured one (Fig. 5*A*). Both model tests and measurements in the northern hemisphere midlatitudes (30–60°N) show elevated oxidized Hg concentrations in the upper troposphere and lower stratosphere (UT/LS). However, the effect of the photoreduction mechanism differs in the upper and lower troposphere. In the lower troposphere (below 5 km), where influence of redox chemistry is smaller, the photoreduction results in a decrease of $Hg^{I,II}$ concentrations. In contrast, in

Table 2. Total Hg lifetime against deposition, mass burden in the troposphere, and statistics of the model evaluation against measurements

Parameter	Obs	Run 1	Run 2	Run 2a	Run 2b
Total Hg^0 mass, Mg	3,856*	1,390	7,865	6,485	8782
Total $Hg^{I,II}$ mass, Mg	359†	127	46	88	20
Hg lifetime against deposition, months		3.5	20	16.3	22.4
Hg^0 concentration					
Mean, ng m^{-3}	1.38 ± 0.25	0.79 ± 0.33	2.75 ± 0.34	2.39 ± 0.36	2.98 ± 0.33
Relative bias, %‡		−42.8	99.0	72.9	115.8
Spatial CC§		0.63	0.69	0.7	0.67
$Hg^{I,II}$ concentration					
Mean, pg m^{-3}	11.7 ± 10.6	32.8 ± 13.9	5.7 ± 4.3	7.2 ± 4.6	4.7 ± 4.2
Relative bias, %		180.9	−51.0	−38.4	−59.3
Spatial CC		0.62	0.05	0.12	0.01
Hg wet deposition					
Mean, g $km^{-2}{\cdot}y^{-1}$	9.1 ± 4.5	8.9 ± 3.0	3.1 ± 1.4	2.0 ± 0.9	0.6 ± 0.3
Relative bias, %		−1.8	−65.6	−77.7	−93.6
Spatial CC		0.58	0.33	0.4	0.2

*Total Hg^0 mass up to 20-km altitude estimated based on the measured vertical profiles of Hg^0 concentration up to 12 km (Fig. 4*A* and *SI Appendix*, Fig. S5*A*) and linear decrease of Hg^0 concentration down to zero at 20 km.
†Total $Hg^{I,II}$ mass up to 20-km altitude estimated based on the aircraft measurement of the vertical profile of $Hg^{I,II}$ concentration (Fig. 4*B* and *SI Appendix*, Fig. S5*B*).
‡Relative bias: $RBIAS = \frac{\overline{M}-\overline{O}}{\overline{O}}100\%$; M and O are modeled and observed values, respectively.
§Pearson's correlation coefficient (CC): $R_{corr} = \frac{\sum_i (M_i-\overline{M})(O_i-\overline{O})}{\sqrt{\sum_i (M_i-\overline{M})^2 \sum_i (O_i-\overline{O})^2}}$.

the UT/LS higher levels of Hg^0 due to the longer lifetime caused by photoreduction (Fig. 5*A*) lead to increased production of oxidized Hg (Fig. 5*B*). It should be noted that both model tests are unable to reproduce the $Hg^{I,II}$ concentration profile throughout the troposphere. This model underestimation of the $Hg^{I,II}$ concentration profile is larger for run 2, even considering the kinetic parameter uncertainties (Fig. 5*B*).

Not including photoreduction of $Hg^{I,II}$ in the model leads to the globally integrated tropospheric predominance of HgBrONO and HgBrOOH among other oxidized Hg species (Fig. 5*C*). At the surface, $HgBr_2$, HgBrOH, and HOHgY also contribute to the modeled Hg^{II} budget in run 1. Implementation of the photoreduction mechanisms drastically changes the composition of oxidized Hg to only HgBrOH (Fig. 5*D*). This results from the combined rapid photolysis of HgBrONO and HgBrOOH to HgBrO (Fig. 1), and the subsequent reaction of the radical with methane to yield HgBrOH (24).

We conducted two further exploratory model runs (Table 1) including an oxidation reaction not to our knowledge documented in the literature ($HgBr + O_3 \rightarrow HgBrO + O_2$, Run#3, see *SI Appendix*, *Supplementary Note 2*) and one simulation in which Br concentrations are increased by a factor of 2 (run 4), to assess the sensitivity of the model results to the uncertainties in tropospheric Br concentrations. The results of these two additional tests, summarized in *SI Appendix*, Table S2, show that the model still overestimates the observed Hg^0 concentration (*SI Appendix*, Fig. S3), although to a smaller extent, and significantly underestimates the measurements of Hg^{II} (*SI Appendix*, Fig. S4) by 40 and 15% for run 3 and run 4, respectively (*SI Appendix*, Table S2). Similarly, wet deposition is still largely underestimated under these exploratory simulations (*SI Appendix*, Fig. S5) as well as the tropospheric concentration profile of Hg^{II} (*SI Appendix*, Fig. S6). The partitioning of oxidized Hg remains

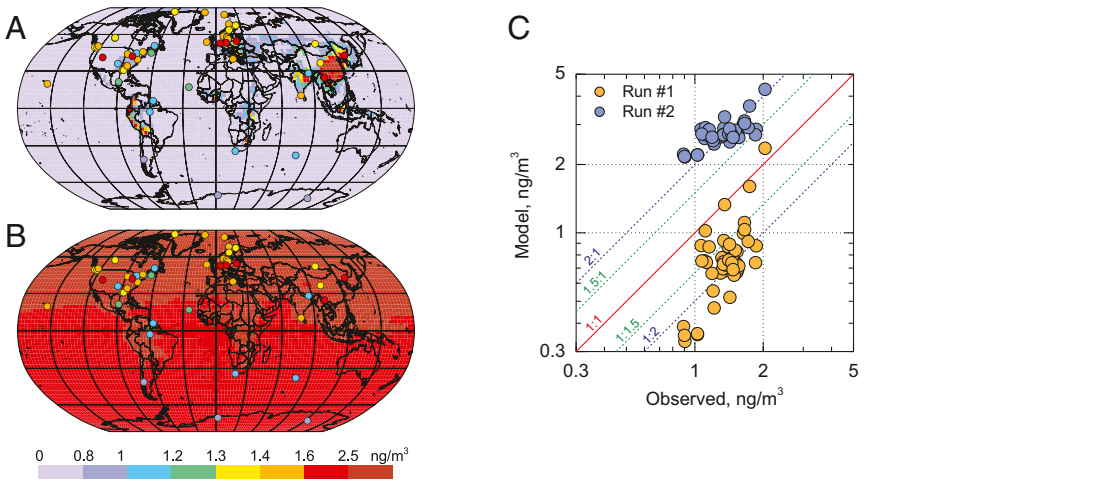

Fig. 2. Comparison of modeled and observed spatial patterns of elemental mercury (Hg^0) concentration in the atmosphere for run 1 (*A*, no photolysis), and run 2 (*B*, $Hg^{I,II}$ photolysis), and scatter plot of the model-to-measurement comparison at ground-based sites (*C*) in 2013.

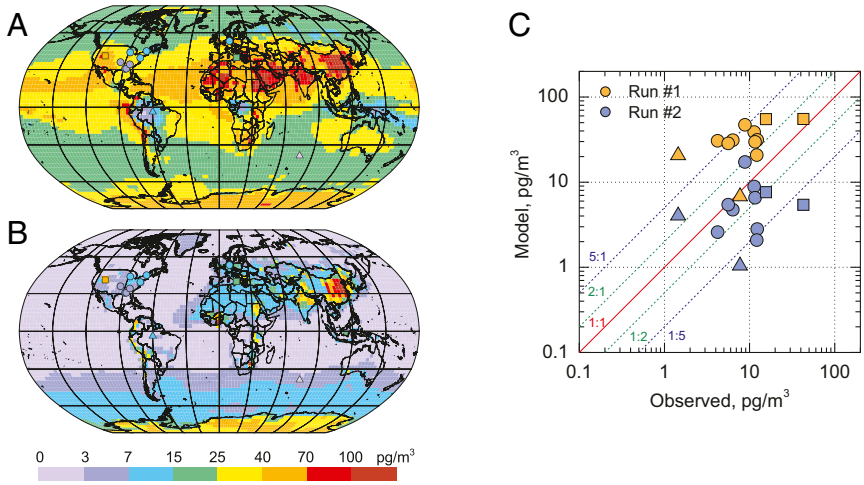

Fig. 3. Comparison of modeled and measured spatial patterns of oxidized mercury (Hg^{I} + Hg^{II}) atmospheric concentrations for run 1 (*A*, no photolysis) and run 2 (*B*, $Hg^{I,II}$ photolysis), and scatter plot of the model-to-measurement comparison at ground-based sites (*C*) in 2013. Circles present sea-level sites in northern midlatitudes; squares, high-elevation sites; triangles, sites in the southern hemisphere.

similar to run 2, with HgBrOH being the predominant species throughout the troposphere (*SI Appendix*, Fig. S6).

In summary, although we acknowledge there are uncertainties in current redox kinetics, Hg^{II} processing in clouds and aqueous aerosols, and in the Br concentrations, our results imply, within the noted uncertainties, a missing Hg^{0} oxidation pathway in the troposphere. This Hg oxidation deficit leads to a calculated unrealistically long Hg^{0} lifetime. Furthermore, implementation of the photoreduction mechanism leads to underestimation of observed Hg^{II} wet deposition. These findings demonstrate that further laboratory, field, and modeling research on the atmospheric chemical cycle of Hg is urgently required.

Methods

Description of the GLEMOS Model. For evaluating the Hg chemical mechanisms under the atmospheric conditions, we apply the three-dimensional multiscale chemical transport model GLEMOS. The model simulates atmospheric transport, chemical transformations, and deposition of Hg species (29, 37). In this study the model grid has a horizontal resolution 3° × 3° and covers troposphere and lower stratosphere up to 10 hPa (~30 km) with 20 irregular terrain-following sigma layers. The atmospheric transport of the tracers is driven by meteorological fields generated by the Weather Research and Forecast modeling system (WRF) (38) fed by the operational analysis data from the European Centre for Medium-Range Weather Forecasts (39). In the current version the model treats Hg^{0}, HgBr, $HgBr_2$, HgBrO, HgBrOH, HgBrOOH, HgBrONO, HOHg, HOHgOOH, and HOHgONO as separate species. Gas-particle partitioning of Hg^{II} is parametrized following Amos et al. (40). Details of the chemical scheme used in the model are given in *SI Appendix*, Table S1. Note that direct formation of the BrHgO radical, from the insertion reaction between Hg^{0} and the BrO radical, was not included in the present mechanism due to the limited experimental and theoretical information available on this reaction (*SI Appendix*, *Supplementary Note 3*). Six-hourly concentration fields of Br are archived from a CAM-Chem simulation (41). Concentrations of OH, HO_2, NO_2, and particulate matter ($PM_{2.5}$) are imported from MOZART (42). We have also included the gas-phase photoreduction of HgBr, HOHg, $HgBr_2$, HgBrOH, HgBrOOH, HgBrONO, HOHgOOH, and HOHgONO using the photolysis rates calculated by CAM-Chem (20, 21, 43) (see *SI Appendix*, *Supplementary Note 4* for $HgBr_2$), including the photolysis yields determined theoretically by multiconfigurational quantum chemistry (24), and an aqueous-phase photoreduction in cloud droplets with a photolysis rate constant 0.153 h^{-1}. We perform simulations for the period 2007–2013 using anthropogenic Hg emissions for 2010 (1) of 1,875 Mg/y. Prescribed fluxes of natural and secondary Hg^{0} reemissions from soil and seawater are generated depending on Hg concentration in soil, soil temperature, and solar radiation for emissions from land and proportional to the primary production of organic carbon in

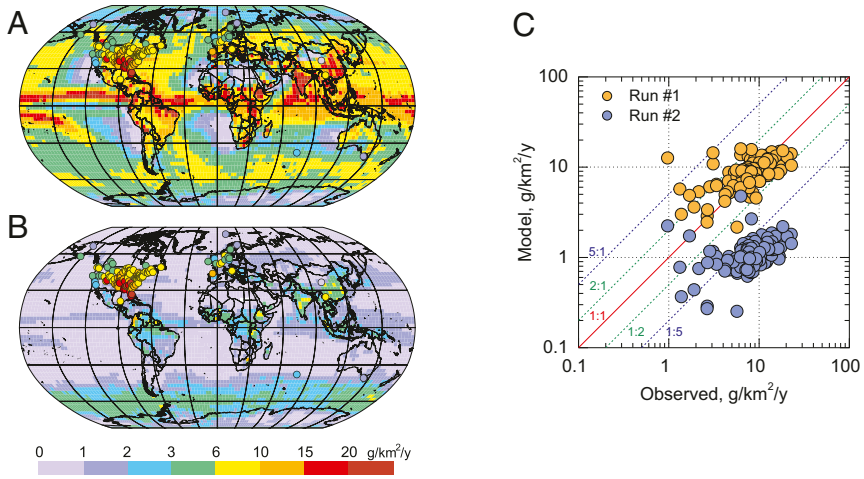

Fig. 4. Comparison of modeled and measured spatial patterns of Hg wet deposition for run 1 (*A*, no photolysis) and run 2 (*B*, $Hg^{I,II}$ photolysis), and scatter plot of the model-to-measurement comparison at ground-based sites (*C*) in 2013.

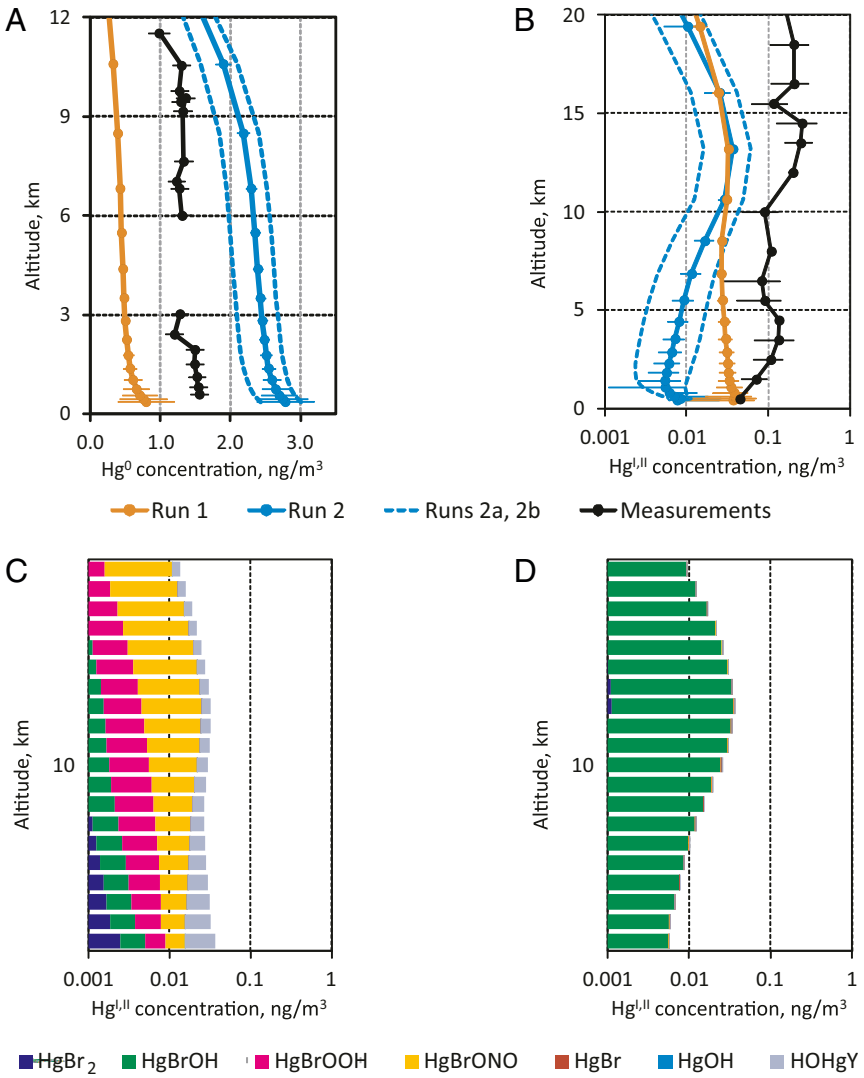

Fig. 5. Modeled and observed vertical profiles of atmospheric concentration of Hg^0 (*A*) and $Hg^{I,II}$ (*B*) over northern midlatitudes; and contribution of various species to $Hg^{I,II}$ concentration for run 1 (*C*, no photolysis) and run 2 (*D*, $Hg^{I,II}$ photolysis).

seawater for emissions from the ocean (37). Additionally, prompt reemission of Hg from snow is taken into account using an empirical parametrization based on the observational data (44–46). Total net evasion of Hg^0 from natural terrestrial and oceanic surfaces varies from 3,050 to 3,200 Mg/y for different tests that is comparable with 3,370 Mg/y of net Hg^0 emission estimated by Horowitz et al. (6). The first 6 y of the period are used for the model spin up to achieve steady-state Hg concentrations in the troposphere. The model results are presented as annual averages for 2013.

Hg^0 and Hg^{II} Observations. The dataset of ground-based Hg^0, Hg^{II}, and Hg^{II} wet deposition observations used in this study is based on the compilation of observations published in Travnikov et al. (29). It contains observations from the Global Mercury Observation System (GMOS) monitoring network (47, 48), the EMEP regional network (49), the Mercury Deposition Network of the National Atmospheric Deposition Program (50), the Atmospheric Mercury Network (51), and the Canadian National Atmospheric Chemistry Database (52, 53). The dataset includes annual mean measurements of Hg^0, Hg^{II}, and Hg^{II} wet deposition flux in 2013. Geographical location of the measurement sites is shown in *SI Appendix*, Fig. S7.

For the dataset of altitudinal Hg^{II} variability, we compiled northern hemisphere midlatitude (30-60°N) aircraft Hg^{II} data from the literature, with observations made by dual-channel oxidized Hg difference methods (17, 54, 55). Gaseous oxidized Hg^{II} observations made by KCl-coated denuder methods (56) were multiplied by 1.56 following ref. (57) for typically observed denuder Hg^{II} loss under free tropospheric conditions (55, 57). Gaseous oxidized Hg^{II} (loss-corrected) and particulate Hg^{II} in the Brooks et al. (56) study were summed to yield total Hg^{II}. The unique, but uncalibrated, stratospheric mean Hg^{II} observations by Murphy et al. (58) were anchored to the Slemr et al. (59) mean Hg^{II} observations for December–May (30–60°N). All available aircraft Hg^{II} data were subsequently binned for 1-km altitude levels, and mean and SDs are shown in *SI Appendix*, Fig. S8.

For the dataset of vertical Hg^0 distribution, we used data from two simultaneous aircraft measurement campaigns in northern Europe. The European Tropospheric Mercury Experiment (ETMEP) measured vertical profiles of the Hg^0 concentration inside the planetary boundary layer and the lower free troposphere in an altitude range of 500–3,500 m (60). The measurements were performed with two collocated Tekran instruments (2537X and 2537B). These were both operated with upstream particle filters and one (2537B) with an additional quartz wool trap to remove oxidized Hg species (54, 61). The experiment was timed in a manner that the data are comparable to observations from the Civil Aircraft for the Regular Investigation of the atmosphere Based on an Instrumented Container project which measured total Hg and Hg^0 in altitudes from 6,000–12,000 m using a Tekran 2537A (62, 63).

Data Availability. All study data are included in the article and *SI Appendix*.

ACKNOWLEDGMENTS. This study has received funding from the European Research Council Executive Agency under the European Union's Horizon

2020 Research and Innovation programme (Project ERC-2016- COG 726349 CLIMAHAL) and the Spanish Ministerio de Economía y Competitividad (MINECO) /Fondo Europeo de Desarrollo Regional (FEDER) (Projects CTQ2017-87054-C2-2-P, RYC-2015-19234, and CEX2019-000919-M). This work was supported by the Consejo Superior de Investigaciones Científicas (CSIC) Spain. A.F.-M. acknowledges the Generalitat Valenciana and the European Social Fund (Contract APOSTD/2019/149 and Project GV/2020/226) for the financial support. J.C.-G. acknowledges the Universitat de València for his Masters Scholarship. M.J. acknowledges funding by the Swiss National Science Foundation (Grant PZ00P2_174101). The ETMEP measurements as well as ground-based measurements of the GMOS network were funded by the EU FP7-ENV-2010 project (GMOS, Grant Agreement 265113). J.S.F. acknowledges the H2020 ERA-PLANET (689443) Integrated Global Observing Systems for Persistent Pollutants (iGOSP) and Integrative and Comprehensive Understanding on Polar Environments (iCUPE) programs.

1. AMAP/UN, Technical Background Report for the Global Mercury Assessment, "2018. Arctic monitoring assessment programme Oslo, Norway/UN environment programme chemical health branch" (Switz, Geneva, 2019).
2. D. Obrist *et al*., A review of global environmental mercury processes in response to human and natural perturbations: Changes of emissions, climate, and land use. *Ambio* **47**, 116–140 (2018).
3. C. T. Driscoll, R. P. Mason, H. M. Chan, D. J. Jacob, N. Pirrone, Mercury as a global pollutant: Sources, pathways, and effects. *Environ. Sci. Technol.* **47**, 4967–4983 (2013).
4. L. Zhang *et al*., A synthesis of research needs for improving the understanding of atmospheric mercury cycling. *Atmos. Chem. Phys.* **17**, 9133–9144 (2017).
5. P. A. Ariya *et al*., Mercury physicochemical and biogeochemical transformation in the atmosphere and at atmospheric interfaces: A review and future directions. *Chem. Rev.* **115**, 3760–3802 (2015).
6. H. M. Horowitz *et al*., A new mechanism for atmospheric mercury redox chemistry: Implications for the global mercury budget. *Atmos. Chem. Phys.* **17**, 6353–6371 (2017).
7. L. Si, P. A. Ariya, Recent advances in atmospheric chemistry of mercury. *Atmosphere (Basel)* **9**, 76 (2018).
8. T. S. Dibble, H. L. Tetu, Y. Jiao, C. P. Thackray, D. J. Jacob, Modeling the OH-initiated oxidation of mercury in the global atmosphere without violating physical laws. *J. Phys. Chem. A* **124**, 444–453 (2020).
9. M. E. Goodsite, J. M. C. Plane, H. Skov, A theoretical study of the oxidation of Hg0 to HgBr2 in the troposphere. *Environ. Sci. Technol.* **38**, 1772–1776 (2004).
10. C. D. Holmes, D. J. Jacob, X. Yang, Global lifetime of elemental mercury against oxidation by atomic bromine in the free troposphere. *Geophys. Res. Lett.* **33**, L20808 (2006).
11. A. Saiz-Lopez, R. von Glasow, Reactive halogen chemistry in the troposphere. *Chem. Soc. Rev.* **41**, 6448–6472 (2012).
12. W. R. Simpson, S. S. Brown, A. Saiz-Lopez, J. A. Thornton, Rv. Glasow, Tropospheric halogen chemistry: Sources, cycling, and impacts. *Chem. Rev.* **115**, 4035–4062 (2015).
13. F. Wang *et al*., Enhanced production of oxidised mercury over the tropical Pacific Ocean: A key missing oxidation pathway. *Atmos. Chem. Phys.* **14**, 1323–1335 (2014).
14. C. D. Holmes *et al*., Global atmospheric model for mercury including oxidation by bromine atoms. *Atmos. Chem. Phys.* **10**, 12037–12057 (2010).
15. S. Wang *et al*., Direct detection of atmospheric atomic bromine leading to mercury and ozone depletion. *Proc. Natl. Acad. Sci. U.S.A.* **116**, 14479–14484 (2019).
16. D. Obrist *et al*., Bromine-induced oxidation of mercury in the mid-latitude atmosphere. *Nat. Geosci.* **4**, 22–26 (2011).
17. L. E. Gratz *et al*., Oxidation of mercury by bromine in the subtropical Pacific free troposphere. *Geophys. Res. Lett.* **42**, 10,494–10,502 (2015).
18. C. N. Gencarelli *et al*., Sensitivity model study of regional mercury dispersion in the atmosphere. *Atmos. Chem. Phys.* **17**, 627–643 (2017).
19. J. M. Pacyna *et al*., Current and future levels of mercury atmospheric pollution on a global scale. *Atmos. Chem. Phys.* **16**, 12495–12511 (2016).
20. A. Saiz-Lopez *et al*., Photoreduction of gaseous oxidized mercury changes global atmospheric mercury speciation, transport and deposition. *Nat. Commun.* **9**, 4796 (2018).
21. A. Saiz-Lopez *et al*., Gas-phase photolysis of Hg(I) radical species: A new atmospheric mercury reduction process. *J. Am. Chem. Soc.* **141**, 8698–8702 (2019).
22. B. de Foy *et al*., First field-based atmospheric observation of the reduction of reactive mercury driven by sunlight. *Atmos. Environ.* **134**, 27–39 (2016).
23. Q. Huang *et al*., Diel variation in mercury stable isotope ratios records photoreduction of PM2.5-bound mercury. *Atmos. Chem. Phys.* **19**, 315–325 (2019).
24. K. T. Lam, C. J. Wilhelmsen, A. C. Schwid, Y. Jiao, T. S. Dibble, Computational study on the photolysis of BrHgONO and the reactions of $BrHgO^{\bullet}$ with CH_4, C_2H_6, NO, and NO_2: Implications for formation of Hg(II) compounds in the atmosphere. *J. Phys. Chem. A* **123**, 1637–1647 (2019).
25. A. Francés-Monerris *et al*., Photodissociation mechanisms of major mercury(II) species in the atmospheric chemical cycle of mercury. *Angew. Chem. Int. Ed.* **59**, 7605–7610 (2020).
26. T. S. Dibble, M. J. Zelie, H. Mao, Thermodynamics of reactions of ClHg and BrHg radicals with atmospherically abundant free radicals. *Atmos. Chem. Phys.* **12**, 10271–10279 (2012).
27. T. S. Dibble, A. C. Schwid, Thermodynamics limits the reactivity of BrHg radical with volatile organic compounds. *Chem. Phys. Lett.* **659**, 289–294 (2016).
28. J. Bieser *et al*., Multi-model study of mercury dispersion in the atmosphere: Vertical and interhemispheric distribution of mercury species. *Atmos. Chem. Phys.* **17**, 6925–6955 (2017).
29. O. Travnikov *et al*., Multi-model study of mercury dispersion in the atmosphere: Atmospheric processes and model evaluation. *Atmos. Chem. Phys.* **17**, 5271–5295 (2017).
30. B. Pal, P. A. Ariya, Studies of ozone initiated reactions of gaseous mercury: Kinetics, product studies, and atmospheric implications. *Phys. Chem. Chem. Phys.* **6**, 572–579 (2004).
31. B. C. Shepler, K. A. Peterson, Mercury monoxide: A systematic investigation of its ground electronic state. *J. Phys. Chem. A* **107**, 1783–1787 (2003).
32. A. J. Hynes, D. L. Donohoue, M. E. Goodsite, I. M. Hedgecock, "Our current understanding of major chemical and physical processes affecting mercury dynamics in the atmosphere and at the air-water/terrestrial interfaces" in *Mercury Fate and Transport in the Global Atmosphere: Emissions, Measurements and Models*, R. Mason, N. Pirrone, Eds. (Springer US, 2009), pp. 427–457.
33. D. A. Jaffe *et al*., Progress on understanding atmospheric mercury hampered by uncertain measurements. *Environ. Sci. Technol.* **48**, 7204–7206 (2014).
34. M. S. Gustin, S. M. Dunham-Cheatham, L. Zhang, Comparison of 4 methods for measurement of reactive, gaseous oxidized, and particulate bound mercury. *Environ. Sci. Technol.* **53**, 14489–14495 (2019).
35. R. Wu, C. Wang, T. S. Dibble, First experimental kinetic study of the atmospherically important reaction of BrHg + NO2. *Chem. Phys. Lett.* **759**, 137928 (2020).
36. D. Khiri, F. Louis, I. Černušák, T. S. Dibble, BrHgO• + CO: Analogue of OH + CO and reduction Path for Hg(II) in the atmosphere. *ACS Earth Space Chem.* **4**, 1777–1784 (2020).
37. O. Travnikov, I. Ilyin, "The EMEP/MSC-E mercury modeling system" in *Mercury Fate and Transport in the Global Atmosphere*, R. Mason, N. Pirrone, Eds. (Springer, Boston, MA, 2009), pp. 571–587.
38. J. G. Skamarock *et al*., A description of the advanced research WRF version 2. NCAR Technical Note, NCAR/TN–468+STR. (National Center Atmospheric Research Boulder Co Mesoscale Microscale Meteorology Div, Boulder, Co) (2005).
39. European Centre for Medium-Range Weather Forecasts, ECMWF operational analysis: Assimilated data. NCAS British Atmospheric Data Centre. http://catalogue.ceda.ac.uk/uuid/c46248046f6ce34fc7660a36d9b10a71. Accessed 11 November 2020.
40. H. M. Amos *et al*., Gas-particle partitioning of atmospheric Hg(II) and its effect on global mercury deposition. *Atmos. Chem. Phys.* **12**, 591–603 (2012).
41. R. P. Fernandez, R. J. Salawitch, D. E. Kinnison, J.-F. Lamarque, A. Saiz-Lopez, Bromine partitioning in the tropical tropopause layer: Implications for stratospheric injection. *Atmos. Chem. Phys.* **14**, 13391–13410 (2014).
42. L. K. Emmons *et al*., Description and evaluation of the model for ozone and related chemical tracers, version 4 (MOZART-4). *Geosci. Model Dev.* **3**, 43–67 (2010).
43. S. P. Sitkiewicz, D. Rivero, J. M. Oliva-Enrich, A. Saiz-Lopez, D. Roca-Sanjuán, Ab initio quantum-chemical computations of the absorption cross sections of HgX_2 and HgXY (X, Y = Cl, Br, and I): Molecules of interest in the Earth's atmosphere. *Phys. Chem. Chem. Phys.* **21**, 455–467 (2018).
44. J. L. Kirk, V. L. St Louis, M. J. Sharp, Rapid reduction and reemission of mercury deposited into snowpacks during atmospheric mercury depletion events at churchill, Manitoba, Canada. *Environ. Sci. Technol.* **40**, 7590–7596 (2006).
45. K. P. Johnson, J. D. Blum, G. J. Keeler, T. A. Douglas, Investigation of the deposition and emission of mercury in arctic snow during an atmospheric mercury depletion event. *J. Geophys. Res. Atmos.* **113**, D17304 (2008).
46. C. P. Ferrari *et al*., Atmospheric mercury depletion event study in Ny-Alesund (Svalbard) in spring 2005. Deposition and transformation of Hg in surface snow during springtime. *Sci. Total Environ.* **397**, 167–177 (2008).
47. F. Sprovieri *et al*., Atmospheric mercury concentrations observed at ground-based monitoring sites globally distributed in the framework of the GMOS network. *Atmos. Chem. Phys.* **16**, 11915–11935 (2016).
48. F. Sprovieri *et al*., Five-year records of mercury wet deposition flux at GMOS sites in the Northern and Southern hemispheres. *Atmos. Chem. Phys.* **17**, 2689–2708 (2017).
49. K. Tørseth *et al*., Introduction to the European Monitoring and Evaluation Programme (EMEP) and observed atmospheric composition change during 1972-2009. *Atmos. Chem. Phys.* **12**, 5447–5481 (2012).
50. E. M. Prestbo, D. A. Gay, Wet deposition of mercury in the U.S. and Canada, 1996–2005: Results and analysis of the NADP mercury deposition network (MDN). *Atmos. Environ.* **43**, 4223–4233 (2009).

51. D. A. Gay *et al*., The atmospheric mercury network: Measurement and initial examination of an ongoing atmospheric mercury record across North America. *Atmos. Chem. Phys.* **13**, 11339–11349 (2013).
52. A. S. Cole *et al*., Ten-year trends of atmospheric mercury in the high Arctic compared to Canadian sub-Arctic and mid-latitude sites. *Atmos. Chem. Phys.* **13**, 1535–1545 (2013).
53. A. Steffen *et al*., Atmospheric mercury in the Canadian Arctic. Part I: A review of recent field measurements. *Sci. Total Environ.* **509–510**, 3–15 (2015).
54. S. N. Lyman, D. A. Jaffe, Formation and fate of oxidized mercury in the upper troposphere and lower stratosphere. *Nat. Geosci.* **5**, 114–117 (2012).
55. P. C. Swartzendruber, D. A. Jaffe, B. Finley, Development and first results of an aircraft-based, high time resolution technique for gaseous elemental and reactive (oxidized) gaseous mercury. *Environ. Sci. Technol.* **43**, 7484–7489 (2009).
56. S. Brooks *et al*., Airborne vertical profiling of mercury speciation near Tullahoma, TN, USA. *Atmosphere (Basel)* **5**, 557–574 (2014).
57. N. Marusczak, J. E. Sonke, X. Fu, M. Jiskra, Tropospheric GOM at the Pic du Midi observatory-correcting bias in denuder based observations. *Environ. Sci. Technol.* **51**, 863–869 (2017).
58. D. M. Murphy, P. K. Hudson, D. Thomson, P. J. Sheridan, J. C. Wilson, Observations of mercury-containing aerosols. *Environ. Sci. Technol.* **40**, 3163–3167 (2006).
59. F. Slemr *et al*., Mercury distribution in the upper troposphere and lowermost stratosphere according to measurements by the IAGOS-CARIBIC observatory: 2014–2016. *Atmos. Chem. Phys.* **18**, 12329–12343 (2018).
60. A. Weigelt *et al*., Tropospheric mercury vertical profiles between 500 and 10 000 m in central Europe. *Atmos. Chem. Phys.* **16**, 4135–4146 (2016).
61. J. L. Ambrose, S. N. Lyman, J. Huang, M. S. Gustin, D. A. Jaffe, Fast time resolution oxidized mercury measurements during the Reno atmospheric mercury intercomparison experiment (RAMIX). *Environ. Sci. Technol.* **47**, 7285–7294 (2013).
62. F. Slemr *et al*., Mercury plumes in the global upper troposphere observed during flights with the CARIBIC observatory from May 2005 until June 2013. *Atmosphere (Basel)* **5**, 342–369 (2014).
63. F. Slemr *et al*., Atmospheric mercury measurements onboard the CARIBIC passenger aircraft. *Atmos. Meas. Tech.* **9**, 2291–2302 (2016).